Article

Soluble porous organic cages as homogenizers and electron-acceptors for homogenization of heterogeneous alloy nanoparticle catalysts with enhanced catalytic activity

Hele Guo [a,b,c,1], Yali Liu [b,1], Hongliang Dong [d,*], Wei Zong [b,e], Kaibin Chu [a,c], Weiwei Li [d], Zhongli Fan [d], Guanjie He [f], Yue-E Miao [b], Ivan P. Parkin [e], Feili Lai [c,g,*], Tianxi Liu [a,*]

[a] Key Laboratory of Synthetic and Biological Colloids, Ministry of Education, School of Chemical and Material Engineering, International Joint Research Laboratory for Nano Energy Composites, Jiangnan University, Wuxi 214122, China
[b] State Key Laboratory for Modification of Chemical Fibers and Polymer Materials, College of Materials Science and Engineering, Donghua University, Shanghai 201620, China
[c] Department of Chemistry, KU Leuven, Leuven 3001, Belgium
[d] Center for High Pressure Science and Technology Advanced Research, Shanghai 201203, China
[e] Christopher Ingold Laboratory, Department of Chemistry, University College London, London WC1H 0AJ, UK
[f] Department of Chemical Engineering, University College London, London WC1E 7JE, UK
[g] Department of Molecular Spectroscopy, Max Planck Institute for Polymer Research, Mainz 55128, Germany

ARTICLE INFO

ABSTRACT

The creation of ultrafine alloy nanoparticles (<5 nm) that can maintain surface activity and avoid aggregation for heterogeneous catalysis has received much attention and is extremely challenging. Here, ultrafine PtRh alloy nanoparticles imprisoned by the cavities of reduced chiral covalent imine cage (PtRh@RCC3) are prepared successfully by an organic molecular cage (OMC) confinement strategy, while the soluble RCC3 can act as a homogenizer to homogenize the heterogeneous PtRh alloy in solution. Moreover, the X-ray absorption near-edge structure (XANES) results show that the RCC3 can act as an electron-acceptor to withdraw electrons from Pt, leading to the formation of higher valence Pt atoms, which is beneficial to improving the catalytic activity for the reduction of 4-nitrophenol. Attributed to the synergistic effect of Pt/Rh atoms and the unique function of the RCC3, the reaction rate constants of Pt_1Rh_{16}@RCC3 are 49.6, 8.2, and 5.5 times than those of the Pt_1Rh_{16} bulk, Pt@RCC3 and Rh@RCC3, respectively. This work provides a feasible strategy to homogenize heterogeneous alloy nanoparticle catalysts in solution, showing huge potential for advanced catalytic application.

© 2022 Science China Press. Published by Elsevier B.V. and Science China Press. All rights reserved.

1. Introduction

In recent years, various single metal materials have been widely used in the fields of catalysis [1–4], sensing [5,6], optics [7,8], and electronics [9,10] due to their unique physical and chemical properties. In order to promote the catalytic performance of single metal nanoparticles, alloying strategy for bimetallic nanoparticles has been regarded as an efficient solution [11–16], which can easily tune the electronic and geometric structures of bimetallic nanoparticles for optimal catalysis performance [17–21]. Additionally, the size of bimetallic nanoparticle also plays a key role in determining their catalytic activity [22–25], as smaller nanoparti-cles lead to higher surface-to-volume ratios and more mismatched atoms on their surfaces, which can create a multitude of defects to improve catalytic activity. Unfortunately, the high surface energy of ultrafine bimetallic nanoparticles makes them thermodynamically unstable to generate agglomerations during both synthetic and catalytic processes. It is an effective strategy to prevent the agglomeration of alloy nanoparticles by employing various ligands or surfactants to protect their outer surface [26,27]. However, the coverage of stabilizer or ligand molecules outside the surface of alloy nanoparticles will greatly limit the exposure of active sites, block the contact between reactants and active centers, and result in decreased catalytic activity. In addition, due to their low price, large specific surface area, and excellent electrical conductivity, carbon materials (e.g., carbon nanotube and graphene) are often used as carriers for dispersing alloy nanoparticles [28,29]. However, alloy nanoparticles will inevitably agglomerate during long-term usage due to the weak interfacial interaction between metal

* Corresponding authors.
E-mail addresses: hongliang.dong@hpstar.ac.cn (H. Dong), feili.lai@kuleuven.be (F. Lai), txliu@jiangnan.edu.cn (T. Liu).
[1] These authors contributed equally to this work.

components and carbon substrates [30]. Therefore, exploring a facile and effective methodology to achieve long-term stable dispersion of alloy nanoparticles is of great significance for improving their applications in catalysis-related fields.

Organic molecular cages (OMCs) are novel and high-profile types of microporous materials with three-dimensional crystalline structures, which are composed of discrete molecules connected by weak interaction forces [31–35]. Apart from the characteristics of traditional organic porous materials (e.g., metal–organic framework and covalent–organic framework), OMCs also possess their own advantages of unique cavity structure, high porosity, inherent open channel, designable molecular structure, and excellent solubility [36,37], which are beneficial to confining the growth of ultrafine alloy nanoparticles with a narrow size distribution, make them physically isolated from each other, and avoid them from significant migration/aggregation. In addition, the high porosity and interconnected channels of OMC can serve as catalytic module spaces for reactant molecules to facilitate mass transfer during the reaction and to provide a powerful platform for various catalytic reactions. Benefiting from the extraordinary solubility of OMCs in solvents, the imprisoned alloy nanoparticles can perform good dispersion in the reaction solvent to enhance their contact with the reactant molecules and accelerate the dynamic process of catalysis [38]. In particular, attributing to the designable molecular structure of OMCs, the coordination between functional groups in the cavity environment and alloy nanoparticles can also be modulated easily to achieve the optimal catalytic property with both high activity and selectivity [39]. Therefore, the confinement strategy by using OMC as porous carrier may be a feasible solution to prepare ultrafine alloy nanoparticles with high activity and stability.

Herein, a facile OMC confinement strategy is presented to synthesize ultrafine PtRh alloy nanoparticles imprisoned by the cavities of reduced chiral covalent imine cage (PtRh@RCC3). Through this soluble RCC3 encapsulation strategy, the heterogeneous catalyst of PtRh alloy nanoparticles can achieve homogenization in solution. Benefiting from the ultrafine particle size and high dispersibility of PtRh alloy nanoparticles in solution, as well as the synergistic enhancement between Pt and Rh metal, the optimized PtRh@RCC3 catalyst exhibits an enhanced activity for the reduction reaction of 4-nitrophenol as compared to those of insoluble Pt_1Rh_{16} bulk and the corresponding single-metal-based nanocomposite catalysts. X-ray absorption near-edge structure (XANES) is carried out to investigate the reasons for the enhanced catalytic performance of PtRh@RCC3, which demonstrates both the alloying strategy and the electron-withdrawing effect of RCC3 can simultaneously lead to a higher oxidation state of the Pt atom for the strong coupling and reduction of 4-nitrophenol to 4-aminophenol.

2. Experimental

2.1. Chemicals

1,3,5-Triformylbenzene (97%), (*R,R*)-1,2-diaminocyclohexane (98%), sodium borohydride ($NaBH_4$, 98%), chloroplatinic acid (H_2PtCl_6, 99.95%) were purchased from Shanghai Titan Technology Co., Ltd. Trifluoroacetic acid (99.5%) and 4-nitropenol (99%) were purchased from Shanghai Macklin Biochemical Co., Ltd. Rhodium chloride hydrate ($RhCl_3\cdot3H_2O$, 98%) was purchased from Bide Pharmatech Ltd. Anhydrous magnesium sulfate ($MgSO_4$, 99.9%) was purchased from Shanghai Wendong Industry and Trade Co., Ltd. Methanol (CH_3OH, AR), ethanol (CH_3CH_2OH, 99.5%), chloroform ($CHCl_3$, AR), and dichloromethane (CH_2Cl_2, AR) were purchased from China National Pharmaceutical Group Corp.

2.2. Synthesis of CC3

The synthesis of chiral covalent imine cage (CC3) was carried out according to a previous method [40]. First, 0.25 g of 1,3,5-triformylbenzene was added to 5 mL of CH_2Cl_2 at room temperature. Second, 5 μL of trifluoroacetic acid was added to the above solution as a catalyst. Third, a CH_2Cl_2 solution (5 mL) containing 0.25 g of (*R,R*)-1,2-diaminocyclohexane was added to the above solution. No stirring was required throughout. Finally, cover the container of the mixed solution and let it stand for one week. The crystals were grown on the vessel walls, separated by filtration, washed with CH_3CH_2OH/CH_2Cl_2 (95:5, v:v) solution, and dried overnight at 70 °C under vacuum.

2.3. Synthesis of RCC3

Reduced chiral covalent imine cage (RCC3) was prepared according to a previous method [41]. The 926 mg of CC3 was first dissolved in a $CH_3OH/CHCl_3$ mixture (1:1, v:v, 50 mL) to form a clear solution. Next, 1.0 g of $NaBH_4$ was added to the above solution and stirred for 12 h at room temperature. After adding 2 mL of deionized water, the solution was stirred for another 12 h. Then, the solvent was removed under vacuum. The obtained white solid was first extracted with $CHCl_3$ (2 × 50 mL) and then the $CHCl_3$ organic phase was washed by water (2 × 100 mL). The $CHCl_3$ organic phase was removed under vacuum after drying with anhydrous $MgSO_4$. RCC3 was purified by a reversible reaction with acetone [41]. The 400 mg of crude RCC3 was dissolved in 40 mL of acetone. After standing for 30 min, crystals began to appear on the wall of the flask, which were collected by filtration after 24 h. The obtained crystals were then dissolved in 40 mL of a $CH_3OH/CHCl_3$ mixture (1:1, v:v) with continuous stirring. The 0.4 mL of deionized water was added to the above solution and stirred for 48 h. Pure RCC3 was obtained after removal of the solvent.

2.4. Synthesis of PtRh@RCC3 catalyst

Typically, 100 mg of purified RCC3 powder was stirred and dissolved in a mixed solution of CH_2Cl_2/CH_3OH (2:1, v:v, 18 mL). Subsequently, different volume of H_2PtCl_6/CH_3OH solution (3 mg mL^{-1}) and $RhCl_3\cdot3H_2O/CH_3OH$ solution (3 mg mL^{-1}) were added to the above solution, and stirred for 3 h to form a homogeneous solution. The molar ratios of H_2PtCl_6 and $RhCl_3\cdot3H_2O$ is designed to be 1:9, 1:16, and 1:25, respectively, and the total metal amount is controlled to be 10 mg. Then, CH_3OH solutions (2 mL) containing 77, 79, and 81 mg of $NaBH_4$, respectively, were immediately added to the above mixed solutions, under ice bath conditions and stirred for 3 h. After that, the products were removed from the solvent under vacuum, washed with deionized water for several times, and dried under vacuum at 70 °C overnight to obtain Pt_1Rh_9@RCC3, Pt_1Rh_{16}@RCC3, and Pt_1Rh_{25}@RCC3 catalysts.

2.5. Synthesis of Pt@RCC3 and Rh@RCC3 catalysts

Pt@RCC3 was synthesized using only H_2PtCl_6. The total Pt amount is controlled to be 10 mg, and the $NaBH_4$ amount was changed to 46 mg. Other synthetic procedures were the same as that of the PtRh@RCC3. The synthesis of Rh@RCC3 uses only $RhCl_3\cdot3H_2O$. The total Rh amount is controlled to be 10 mg, and the $NaBH_4$ amount was changed to 83 mg. Other synthetic procedures were the same as that of the PtRh@RCC3.

2.6. Synthesis of Pt bulk, Rh bulk, and various PtRh bulk catalysts

Pt bulk was prepared via the same steps as Pt@RCC3 without adding RCC3 powder. Rh bulk was prepared via the same steps

as Rh@RCC3 without adding RCC3 powder. PtRh bulk samples including Pt_1Rh_9 bulk, Pt_1Rh_{16} bulk, and Pt_1Rh_{25} bulk were prepared via the same steps as PtRh@RCC3 without adding RCC3 powder.

2.7. Procedure for the reduction of 4-nitrophenol

The catalytic activities of various prepared catalysts were tested under liquid-phase ambient conditions by using the hydrogenation reduction of 4-nitrophenol as the verification reaction ($NaBH_4$ is used as the reducing agent). First, 2.5 mg of $NaBH_4$ and 4 mL of a 4-nitrophenol (0.1 mmol L^{-1}) in CH_2Cl_2/CH_3OH mixture solution (2:1, v:v) was mixed in a cell. Then, 0.2 mg of catalyst was added to the above solution. After introducing the catalyst, the bright yellow solution gradually faded as the reaction proceeded. Ultraviolet–visible (UV–vis) spectra were recorded at short intervals to monitor the progress of the reaction. The absorption spectra of the solution were measured in the range of 250–500 nm. The rate constant k for the reduction of 4-nitrophenol can be determined by measuring the absorbance at wavelength λ = 400 nm as a function of reaction time.

2.8. Characterization

X-ray diffraction (XRD) patterns were measured using an X'Pert Pro X-ray diffractometer equipped with Cu Kα radiation (λ = 0.1542 nm) at a current of 40 mA and voltage of 40 kV. The ^1H and ^{13}C nuclear magnetic resonance (NMR) were measured by a Bruker AVANCE III HD 600 MHz instrument. The Fourier transform infrared (FTIR) spectra were measured with a Nicolet Impact 410 Fourier transform infrared spectrometer. Thermogravimetric analysis (TGA) was carried out by a TG 209 F1 Libra thermal analyzer at a heating rate of 20 °C min^{-1} in the temperature range of 35–800 °C under air. The N_2 adsorption/desorption isotherms were collected at liquid nitrogen temperature (77 K) using a QUADRASORB SI automated surface area and pore size analyzer (Quantachrome Corporation). The specific surface area was calculated from the adsorption data according to the Brunauer-Emmett-Teller (BET) method. The X-ray photoelectron spectroscopy (XPS) was analyzed on a Karatos Axis ULTRA X-ray photoelectron spectrometer instrument. The morphologies of samples were examined by using field-emission scanning electron microscopy (SEM, JEOL JSM-7001F) and transmission electron microscopy (TEM, TALOS F200S). UV–vis spectroscopy was recorded by a UV–vis spectrophotometer (Lambda-35). The X-ray absorption spectra (XAS) of Pt L_3 edge were conducted at BL14W1 beamline of Shanghai Synchrotron Radiation Facility (SSRF). The acquired extended X-ray absorption fine structure spectra (EXAFS) data was processed according to the standard procedures using the ATHENA module of Demeter software packages. Subsequently, the $\chi(k)$ data was Fourier transformed to real (R) space using a Hanning windows (dk = 1.0 $Å^{-1}$) to separate the EXAFS contributions from different coordination shells. To obtain the quantitative structural parameters around central atoms, least-squares curve parameter fitting was performed using the ARTEMIS module of Demeter software packages.

3. Results and discussion

3.1. Synthesis and characterization of PtRh@RCC3

Fig. 1a demonstrates that alloy catalysts prepared by traditional strategy tend to agglomerate in solution, which can greatly hinder the exposure of active sites. To overcome this issue, a soluble organic molecular cage (OMC) confinement strategy is proposed

to homogenize the alloy nanoclusters in solution, as shown in Fig. 1b. The amine cage RCC3 that has good solubility in organic solvents was chosen as the stabilizer and homogenizer for the highly dispersed PtRh nanoparticles. The synthetic route of the RCC3 is shown in Fig. S1 (online). Firstly, a high-purity organic crystal of chiral covalent imine cages (CC3) (structural details are shown in Fig. S2 online) was obtained by the imine cyclization reaction of 1,3,5-triformylbenzene and (*R,R*)-1,2-diaminocyclohexane by catalytic assistance of trifluoroacetic acid [40]. The CC3 with unsaturated double bonds were then reduced by reducing agent $NaBH_4$ to obtain highly stable RCC3. The ^1H and ^{13}C NMR analysis of the RCC3 suggests their structural integrity and successful preparation in high purity (Fig. S3 online) [41,42]. Subsequently, the PtRh alloy nanoparticles were encapsulated in the cavity of the RCC3 by immersing the RCC3 in the Pt^{4+}/Rh^{3+}-containing CH_2Cl_2/CH_3OH solution, during which an *in-situ* reduction process occurred with the assistance of $NaBH_4$ as a reducing agent (Fig. 1b). After the reduction reaction, the solvent was removed from the mixed solution under vacuum and washed with deionized water to obtain PtRh@RCC3 powder. The PtRh@RCC3 with Pt^{4+}/Rh^{3+} molar ratios of 1/9, 1/16, and 1/25 were prepared and denoted as Pt_1Rh_9@RCC3, Pt_1Rh_{16}@RCC3, and Pt_1-Rh_{25}@RCC3, respectively. Another two control samples of Pt@RCC3 and Rh@RCC3 were also prepared with addition of only Pt^{4+} or Rh^{3+} ions, respectively.

As XRD patterns of various samples shown in Fig. 1c and Fig. S4 (online), the samples of metal nanoparticles encapsulated by RCC3 (Pt@RCC3, Rh@RCC3, and PtRh@RCC3) present the sharp crystalline diffraction peaks (10°–25°) as the same as RCC3, indicating that RCC3 retains its intact structure after encapsulating metal or alloy nanoparticles. Moreover, no characteristic diffraction peaks of Pt metal, Rh metal, and PtRh alloys can be observed in Pt@RCC3, Rh@RCC3, and PtRh@RCC3 nanocomposites, respectively, which is mainly due to the confinement effect of RCC3 resulting in the formation of homogeneous ultrafine alloy or metal nanoparticles. Fig. 1d and Fig. S5 (online) present the FTIR spectra of Pt@RCC3, Rh@RCC3, and various PtRh@RCC3 nanocomposites without obvious differences, which indicates that the covalent bond of RCC3 remains complete after encapsulating metals species in RCC3. To be noted, a slight red shift of the stretching vibration peak of –C–N– in RCC3 can be observed from 1116.3 to 1119.0 cm^{-1} after the encapsulation of metal/alloy nanoparticle, which is mainly attributed to the formation of metal–N bonds [43]. The metal contents of various PtRh@RCC3 samples, as well as contrast samples of Pt@RCC3 and Rh@RCC3, were confirmed by TGA to be approximately 6.3 wt% (Fig. 1e and Fig. S6 online), indicating the similar metal loadings in these samples. Besides, the BET specific surface areas of RCC3, Pt_1Rh_{16}@RCC3, Pt@RCC3, Rh@RCC3, and Pt_1Rh_{16} bulk were investigated by nitrogen adsorption-desorption isotherms, as shown in Fig. S7 (online). The Pt_1Rh_{16}@RCC3, Pt@RCC3, and Rh@RCC3 samples exhibit similar specific surface areas of 190.65, 178.81, and 183.29 m^2 g^{-1}, respectively, which are lower than that of RCC3 cage (457.31 m^2 g^{-1}), but much higher than that of Pt_1Rh_{16} bulk (41.38 m^2 g^{-1}).

3.2. Morphology and components analysis

Fig. 2a shows the field emission scanning electron microscopy (FESEM) image of Pt_1Rh_{16}@RCC3. The Pt_1Rh_{16}@RCC3 exhibits a spherical morphology with a size of about 500 nm. TEM image of Pt_1Rh_{16}@RCC3 shows that PtRh alloy nanoparticles are uniformly dispersed inside the RCC3 matrix with a size of about 2.5 nm (Fig. 2b, c). The high-resolution TEM image shows the interplanar spacing of PtRh alloy nanoparticles is about 0.223 nm (insert of Fig. 2b), which is between the interplanar spacings of Pt and Rh monometals [44], indicating the successful formation of PtRh alloy
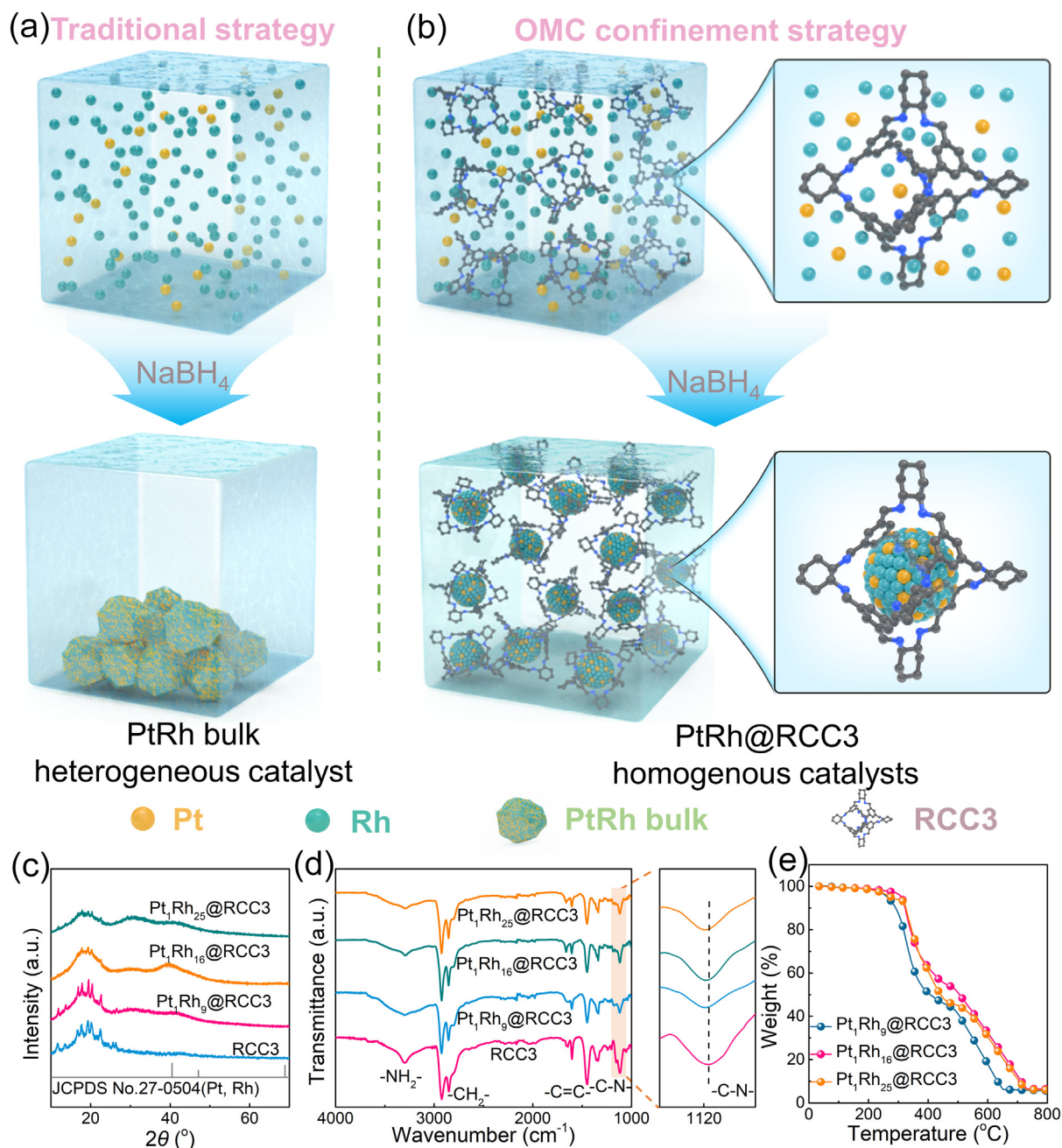
Fig. 1. Preparation and characteristics of PtRh@RCC3. (a) Schematic illustrations of traditional strategy for synthesizing heterogeneous PtRh bulk, and (b) OMC confinement strategy for preparing homogenous PtRh@RCC3 catalysts. (c) XRD patterns, (d) FTIR spectra, and (e) TGA profiles of RCC3 and PtRh@RCC3 with different Pt/Rh ratios.

nanoparticles in PtRh@RCC3. High-angle annular dark-field scanning TEM (HAADF-STEM) image of the Pt$_1$Rh$_{16}$@RCC3 nanocomposite and corresponding energy-dispersive X-ray spectroscopy (EDS) elemental mappings confirm the homogeneous distributions and good alloying property of PtRh nanoparticles within the skeleton of RCC3 (Fig. 2d). The peaks of Pt and Rh also appear in the corresponding energy spectrum (Fig. 2e).

In addition, the chemical compositions of PtRh@RCC3 nanocomposites were further studied by XPS technique. In the full XPS spectra of Pt$_1$Rh$_{16}$@RCC3 (Fig. S8 online), almost no Pt and Rh characteristic peaks can be observed, which is mainly due to the low content of PtRh nanoparticles. High-resolution N 1s spectra of RCC3 and PtRh@RCC3 nanocomposites show pyridinic-N and pyrrolic-N species at 398.7 and 400.1 eV, respectively (Fig. 2f)

[45–47]. For the high-resolution Pt 4f spectra (Fig. 2g), the binding energies of Pt 4f in PtRh@RCC3 nanocomposites show shifts toward higher values relative to Pt@RCC3 [48]. In contrast, the binding energies of Rh 3d in PtRh@RCC3 nanocomposites show shifts toward lower values relative to Rh@RCC3 (Fig. 2h). These results indicate the presence of some alloying interactions between Pt and Rh, as well as electron transfer from Pt to Rh that is beneficial for substantially improving the catalytic efficiency [48].

3.3. Catalytic tests for the reduction of 4-nitrophenol to 4-aminophenol

To evaluate the catalytic enhancement of the prepared PtRh@RCC3 catalyst in the liquid phase reaction, the reduction of 4-nitrophenol to 4-aminophenol by NaBH$_4$ is used as the test reac-
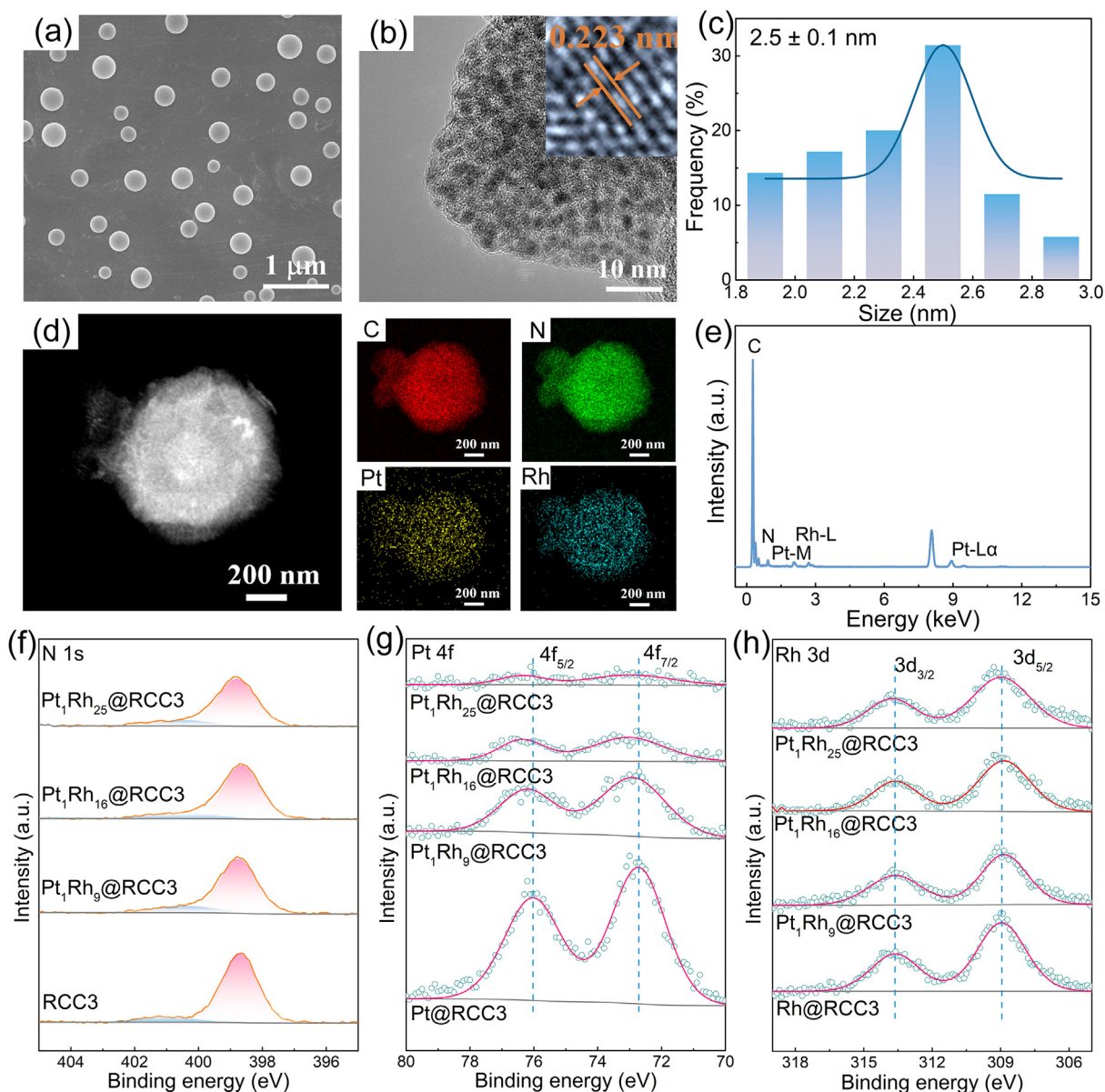
Fig. 2. Morphology and composition characterizations of PtRh@RCC3 samples. (a) SEM image and (b) TEM image of Pt$_1$Rh$_{16}$@RCC3. (c) Particle size distribution histogram of PtRh alloys in Pt$_1$Rh$_{16}$@RCC3. (d) HAADF-STEM of Pt$_1$Rh$_{16}$@RCC3 and the corresponding EDS elemental mapping of C, N, Pt, and Rh. (e) EDS spectrum of Pt$_1$Rh$_{16}$@RCC3. (f) High-resolution N 1s spectrum of RCC3 and various PtRh@RCC3 nanocomposites. (g) High-resolution Pt 4f XPS spectrum of Pt@RCC3 and various PtRh@RCC3 nanocomposites. (h) High-resolution Rh 3d XPS spectrum of Rh@RCC3 and various PtRh@RCC3 nanocomposites.

tion. The change of the absorption peak intensity of 4-nitrophenol was monitored by UV–vis spectroscopy. The absorption peak of 4-nitrophenol solution shows a red shift from 317 to 400 nm after the addition of freshly prepared NaBH$_4$ solution (Fig. S9 online), which is due to the appearance of 4-nitrophenol ions induced by NaBH$_4$ in an alkaline environment [49]. Moreover, even after 1 h of holding, the 4-nitrophenol/NaBH$_4$ solution showed a negligible decrease in the intensity of the absorption peak at 400 nm, indicating that it hardly undergoes reduction in the absence of any catalyst (Fig. S10 online). Fig. 3a shows that the color of the 4-nitrophenol solution changed from colorless to bright yellow after the addition of NaBH$_4$, and the color gradually weakened from bright yellow to colorless after the addition of the catalyst, suggesting the occurrence of the reduction reaction of 4-nitrophenol. As the reaction progressed, the absorbance of reactant 4-nitrophenol at 400 nm decreased, while the absorbance of pro-

duct 4-aminophenol at 300 nm increased. As shown in Fig. 3b and Figs. S12–S14 (online), Pt$_1$Rh$_{16}$@RCC3 catalysts exhibit the fastest reduction rate of 4-nitrophenol and can completely convert 4-nitrophenol within 6 min, while Pt$_1$Rh$_9$@RCC3 and Pt$_1$Rh$_{25}$@-RCC3 catalysts require 12 and 10 min, respectively. The kinetics of the reduction of 4-nitrophenol can be described by the following linear equation: $-kt = \ln(A_t/A_0)$, where A_t and A_0 refer to the absorbance values at the interval and initial stages, respectively [50,51]. The rate constant (k) of Pt$_1$Rh$_{16}$@RCC3 is 0.843 min^{-1}, which is higher than those of Pt$_1$Rh$_9$@RCC3 (0.374 min^{-1}) and Pt$_1$Rh$_{25}$@-RCC3 (0.442 min^{-1}). To evaluate the improvement effect of alloying strategy on the catalytic reduction activity of 4-nitrophenol, Pt@RCC3 and Rh@RCC3 nanocomposites were also employed as catalysts for the reduction of 4-nitrophenol. When compared with the PtRh@RCC3 catalysts, the complete conversion of 4-nitrophenol to 4-aminophenol by Pt@RCC3 and Rh@RCC3
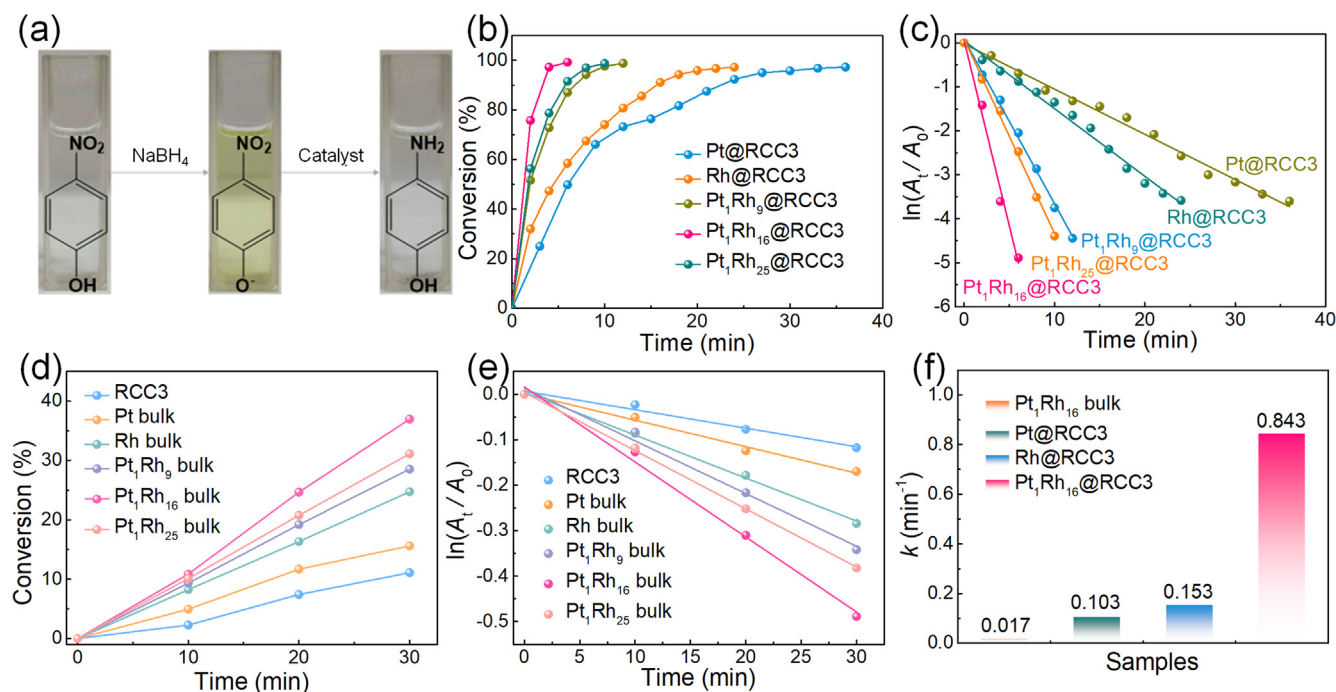
Fig. 3. Performance of the catalytic reduction of 4-nitrophenol to 4-aminophenol. (a) Color change during the reduction of 4-nitrophenol. (b) Comparative catalytic conversion of 4-nitrophenol over Pt@RCC3, Rh@RCC3, various PtRh@RCC3 catalysts. (c) Plots of $\ln(A_t/A_0)$ of Pt@RCC3, Rh@RCC3, various PtRh@RCC3 catalysts for the absorbance of 4-nitrophenol at 400 nm versus reaction time. (d) Comparative catalytic conversion of 4-nitrophenol over RCC3, Pt bulk, Rh bulk and various PtRh bulk catalysts. (e) Plots of $\ln(A_t/A_0)$ of RCC3, Pt bulk, Rh bulk and various PtRh bulk catalysts for the absorbance of 4-nitrophenol at 400 nm versus reaction time. (f) Comparison of rate constants (k) of Pt_1Rh_{16}@RCC3, Pt@RCC3, Rh@RCC3 and Pt_1Rh_{16} bulk catalysts.

require much longer time of 36 and 24 min, with corresponding k values of 0.103 and 0.153 min^{-1}, respectively (Fig. 3b, c and Figs. S15, S16 online). These results demonstrate that the formation of alloy nanoparticles with strong bimetallic interaction is favorable to improve the catalytic efficiency due to their synergistic effect. Furthermore, insoluble Pt bulk, Rh bulk and various PtRh bulks (Pt_1Rh_{16}, Pt_1Rh_9, and Pt_1Rh_{25} bulks) were also prepared without the addition of RCC3 cages and used as the catalysts for the reduction of 4-nitrophenol to investigate the importance of the confinement and homogenization effects of RCC3 cage. The insoluble Pt, Rh, Pt_1Rh_9, Pt_1Rh_{16}, and Pt_1Rh_{25} bulks can only convert a small part of 4-nitrophenol (<40%) even if the reaction time is extended to 30 min, and their corresponding k values are all below 0.015 min^{-1}, respectively (Fig. 3d, e and Figs. S17–S21 online). In addition, the catalytic reduction reaction of 4-nitrophenol by RCC3 was also tested, and the results show that it has basically no catalytic ability (Fig. S22 online), which indicates that it only acts as a support in the catalytic process. As compared with the Pt bulk, Rh bulk, and various PtRh bulk catalysts, all of the soluble Pt@RCC3, Rh@RCC3, and various PtRh@RCC3 homogeneous catalysts exhibit significantly increased k values for the reduction of 4-nitrophenol (Fig. S23 online), demonstrating that the homogenization of metal species by RCC3 can significantly improve the catalytic performance. Among the various prepared catalysts, the soluble Pt_1Rh_{16}@RCC3 homogeneous catalyst shows the best catalytic performance towards the reduction of 4-nitrophenol, and its k value is 49.6, 8.2, and 5.5 times than those of Pt_1Rh_{16} bulk, Pt@RCC3, and Rh@RCC3, respectively (Fig. 3f). In addition, the surface area normalized k value (k/S) of the Pt_1Rh_{16}@RCC3 catalyst was 10.8, 7.7, and 5.3 times those of the Pt_1Rh_{16} bulk, Pt@RCC3, and Rh@RCC3 (Fig. S24 online), indicating that the appropriate alloying between Pt and Rh atoms and the homogenization of the RCC3 cages on the PtRh alloy nanoparticles can greatly contribute to the catalytic performance. Furthermore, compared with various

recently reported metal nanoparticle/support catalysts, our Pt_1-Rh_{16}@RCC3 catalyst shows better 4-nitrophenol reduction performance than most catalysts (Table S1 online), indicating that the soluble molecular cage RCC3 is an ideal carrier for the preparation of efficient 4-nitrophenol reduction catalysts.

To further demonstrate the stabilizing effect of RCC3 on PtRh alloy nanoparticles, we collected and characterized the as-obtained Pt_1Rh_{16}@RCC3 catalyst after 4-nitrophenol reduction catalysis. Fig. S25 (online) shows the XRD pattern of Pt_1Rh_{16}@RCC3 after catalysis, some sharp crystalline diffraction peaks between 10°–25° correspond well with the RCC3, indicating that RCC3 retains its intact structure after catalysis. In addition, no characteristic diffraction peaks were observed for PtRh alloys, further suggesting that no significant nanoparticle agglomeration occurred during the 4-nitrophenol reduction process. TEM images of Pt_1-Rh_{16}@RCC3 after catalysis show that PtRh alloy nanoparticles are still homogeneously dispersed inside the RCC3 matrix without agglomeration (Fig. S26a, b online). High-resolution TEM images show that the planar spacing of PtRh alloy nanoparticles remains at 0.223 nm (inset of Fig. S26b online). HAADF-STEM image of Pt_1-Rh_{16}@RCC3 after catalysis and its corresponding EDS elemental mappings demonstrate that the PtRh nanoparticles in the RCC3 skeleton still exhibit good alloying properties (Fig. S26c online). All the above results indicate that the Pt_1Rh_{16}@RCC3 catalyst has excellent structural stability.

3.4. X-ray absorption spectra to examine the interaction between RCC3 and PtRh nanoparticles

To further explore the electronic coupling effect of RCC3 and PtRh alloy nanoparticles and elucidate its effect on the catalytic performance of 4-nitrophenol reduction, XANES measurements were performed on Pt foil, Pt_1Rh_{16} bulk, and Pt_1Rh_{16}@RCC3. The white line intensity of the Pt L$_3$-edge normalized XANES is a qual-
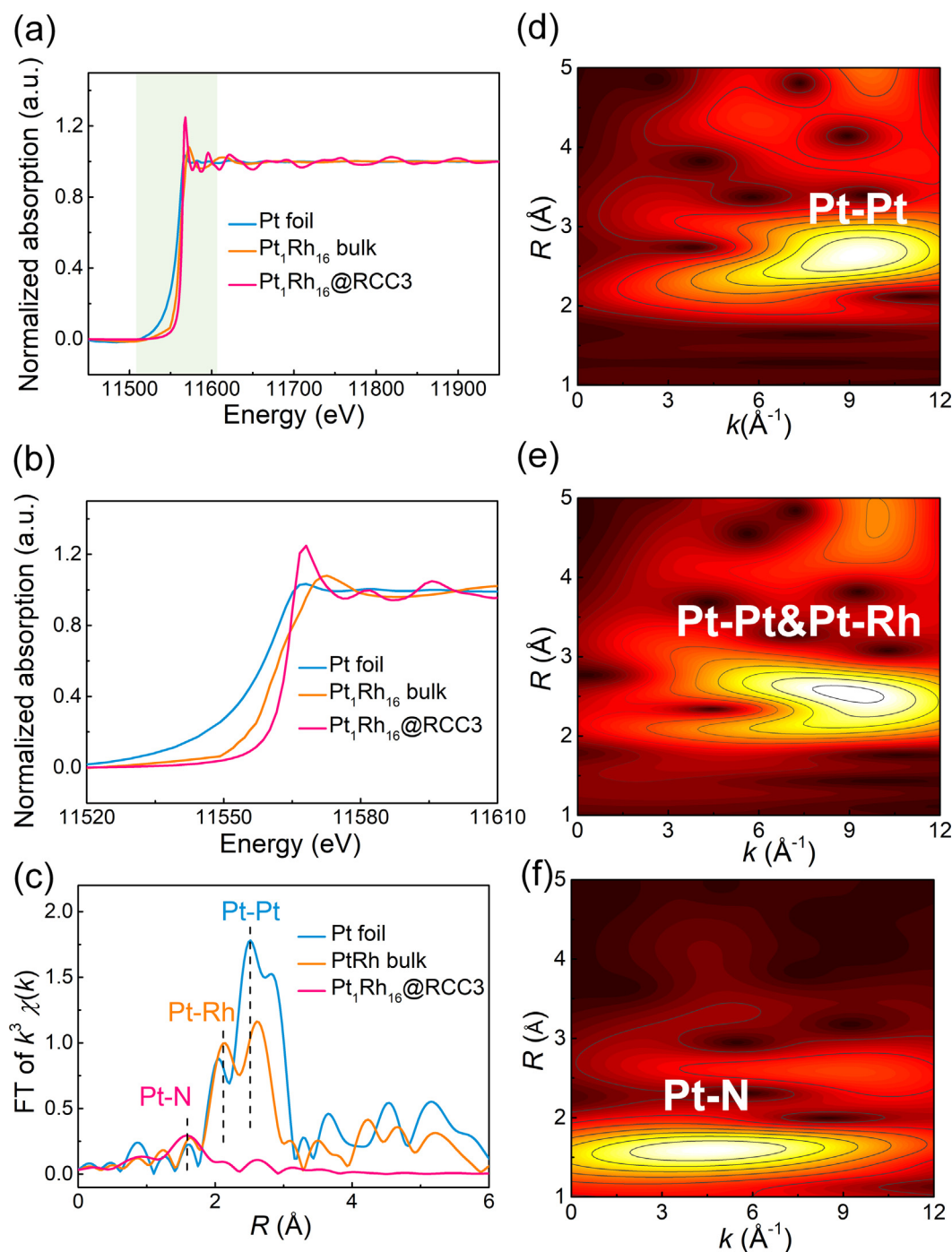
Fig. 4. XAS characterizations of the Pt_1Rh_{16} bulk and Pt_1Rh_{16}@RCC3. (a, b) The normalized XANES spectra at the Pt L_3 edge of Pt foil, Pt_1Rh_{16} bulk, and Pt_1Rh_{16}@RCC3. (c) FT-XANES spectra at the Pt L_3 edge of Pt foil, Pt_1Rh_{16} bulk, and Pt_1Rh_{16}@RCC3. WT-EXAFS for (d) Pt foil, (e) Pt_1Rh_{16} bulk, and (f) Pt_1Rh_{16}@RCC3.

itative indicator of the *d*-band vacancy [52,53]. The Pt L_3-edge white line intensity of PtRh alloy is higher than that of Pt foil (Fig. 4a, b), indicating that the former has more Pt *d*-band vacancies and therefore produces more positively charged Pt centers. In addition, the Pt L_3-edge white line intensity of Pt_1Rh_{16}@RCC3 is also higher than that of the Pt_1Rh_{16} bulk, indicating that RCC3 can act as an electron acceptor to extract electrons from Pt atoms to form higher valence Pt atoms. The EXAFS were used to further determine the coordination environment of Pt atoms in the Pt_1Rh_{16}@RCC3 catalyst. The EXAFS fitting curves at *R*-space and *k*-space are consistent with the experiment spectra of Pt foil, Pt_1-

Rh_{16} bulk, and Pt_1Rh_{16}@RCC3, respectively (Figs. S27, S28 online). The Fourier transforms of the EXAFS (FT-EXAFS) of Pt foil, Pt_1Rh_{16} bulk, and Pt_1Rh_{16}@RCC3 are displayed in Fig. 4c. Due to the low content of Pt atoms in the Pt_1Rh_{16} bulk and Pt_1Rh_{16}@RCC3 catalysts, their peak heights around 2.6 Å are significantly lower than those of the Pt foil. Besides, the contributions of Pt–Rh and Pt–Pt bonds in the Pt_1Rh_{16} bulk lead to distinct split peaks between at 2.1 and 2.6 Å [54]. In particular, a main broad peak at around 1.6 Å, which is far from the Pt–Pt and Pt–Rh bonds, can be clearly observed in the Pt_1Rh_{16}@RCC3 catalyst. This is mainly attributed to the coordination between the N elements of the RCC3 and the Pt
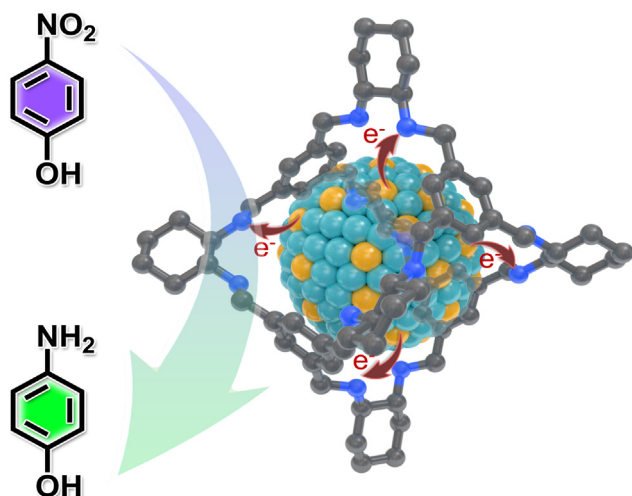
Fig. 5. Schematic illustration of the 4-nitrophenol catalytic reduction on the PtRh@RCC3 catalyst.

atoms of PtRh nanoparticles, which induces the formation of a Pt-N shell layer on the surface of the PtRh nanoparticles. The wavelet transform of $c(k)$ (WT)-EXAFS is an intuitive way to demonstrate the properties of adjacent Pt atoms (Fig. 4d–f). The Pt foil shows a distinct scattering path signals at $[\chi(k), \chi(R)]$ of [9.1, 2.52], which are associated with the Pt-Pt path (Fig. 4d). The intensity of the Pt-Pt path signal in the Pt_1Rh_{16} bulk attenuates, while the signal of the scattering path located at [7.6, 2.11] enhances that is caused by the Pt-Rh path (Fig. 4e). Moreover, Pt_1Rh_{16}@RCC3 catalyst displays a scattering path signal at [4.2, 1.60] corresponding to the Pt-N paths, further proving the formation of a Pt-N shell within Pt_1-Rh_{16}@RCC3 (Fig. 4f).

Fig. 5 briefly describes the scheme of the 4-nitrophenol catalytic reduction on the PtRh@RCC3. The prominent 4-nitrophenol reduction performance on the Pt_1Rh_{16}@RCC3 catalyst can be explained as follows: (1) proper alloying between Pt and Rh atoms can easily tune the electronic and geometric structures of bimetallic nanoparticles, thus achieving optimal catalytic performance; (2) the RCC3 with high porosity and interconnected channels can act as structural stabilizers to constrain the growth of ultrafine PtRh alloy nanoparticles, isolate them from each other physically, and avoid their apparent aggregation, thereby greatly facilitating mass transfer during the reaction; (3) the extraordinary solubility of RCC3 in the solvent makes it a homogenizer for the heterogeneous PtRh alloy catalysts, which endows the PtRh alloy with good dispersibility in the reaction solution, enhances their contact with the reactant molecules, and thus accelerates the dynamic process of catalysis; (4) due to the abundant polar functional groups, RCC3 can act as an electron-acceptor to extracts electrons from Pt in PtRh alloy nanoparticles for the formation of higher-valence Pt atoms, thereby enhancing its intrinsic catalytic activity significantly.

4. Conclusion

In summary, an efficient impregnation method is proposed to encapsulate PtRh alloy nanoparticles in the cavity of soluble RCC3 to obtain PtRh@RCC3 catalysts. The *in-situ* formed PtRh bimetallic alloy nanoparticles in the cavity of RCC3 show outstanding dispersion in the reaction solution and good alloying properties with an average particle size of 2.5 nm. By taking the reduction of 4-nitrophenol as an example, the catalytic performance of PtRh@RCC3 has been investigated in detail, where the optimized

Pt_1Rh_{16}@RCC3 exhibits the highest activity. Its reaction rate constant is 49.6, 8.2, and 5.5 times those of insoluble heterogeneous PtRh alloy and the single-metal counterparts (Pt@RCC3 and Rh@RCC3), respectively. These results strongly suggest that the synergistic effect of bimetals, as well as the homogenization and confinement effects of RCC3, can greatly enhance the catalytic activity of PtRh@RCC3 catalyst. The Pt L_3-edge electronic structures of PtRh@RCC3 and PtRh bulk are further analyzed by XANES, and the results show that the Pt element in the PtRh@RCC3 has the highest degree of oxidation, which is beneficial to modulating and improving the effectiveness for the catalytic reduction of 4-nitrophenol. Homogenizing alloy nanoparticles in solution with soluble molecular cages as homogenizers and electron acceptors provide a new perspective for the development of advanced nanometal-based catalysts for various catalytic fields including electrocatalysis, photocatalysis, and thermocatalysis.

Conflict of interest

The authors declare that they have no conflict of interest.

Author contributions

Feili Lai and Tianxi Liu contributed to the concepts and design of the investigation. Hele Guo, Yali Liu, Hongliang Dong, Wei Zong, Kaibin Chu, Weiwei Li, and Zhongli Fan carried out all sample synthesis and characterization. Hele Guo and Yali Liu wrote the manuscript. Hongliang Dong, Guanjie He, Yue-E Miao, and Ivan P. Parkin contributed to the overall scientific interpretation and revised this paper.

Appendix A. Supplementary materials

Supplementary materials to this article can be found online at https://doi.org/10.1016/j.scib.2022.11.010.

References

[1] Carlier S, Gripekoven J, Philippo M, et al. Ru on N-doped carbon supports for the direct hydrogenation of cellobiose into sorbitol. Appl Catal B-Environ 2021;282:119515.

[2] Li L, Cai J, Liu Y, et al. Zeolite-seed-directed Ru nanoparticles highly resistant against sintering for efficient nitrogen activation to ammonia. Sci Bull 2020;65:1085–93.

[3] Hao J, Zhuang Z, Cao K, et al. Unraveling the electronegativity-dominated intermediate adsorption on high-entropy alloy electrocatalysts. Nat Commun 2022;13:2662.

[4] Wong A, Liu Q, Griffin S, et al. Synthesis of ultrasmall, homogeneously alloyed, bimetallic nanoparticles on silica supports. Science 2017;358:1427–30.

[5] Liu X, Astruc D. From galvanic to anti-galvanic synthesis of bimetallic nanoparticles and applications in catalysis, sensing, and materials science. Adv Mater 2017;29:1605305.

[6] Potyrailo RA. Toward high value sensing: monolayer-protected metal nanoparticles in multivariable gas and vapor sensors. Chem Soc Rev 2017;46:5311–46.

[7] Nguyen L, Dass M, Ober MF, et al. Chiral assembly of gold-silver core-shell plasmonic nanorods on DNA origami with strong optical activity. ACS Nano 2020;14:7454–61.

[8] Wu F, Guo J, Huang Y, et al. Plexcitonic optical chirality: strong exciton-plasmon coupling in chiral j-aggregate-metal nanoparticle complexes. ACS Nano 2021;15:2292–300.

[9] Kumar D, Tibbitts L, Newell J, et al. Evaluating differences in the active-site electronics of supported Au nanoparticle catalysts using hammett and DFT studies. Nat Chem 2018;10:268–74.

[10] Yan Y, Warren SC, Fuller P, et al. Chemoelectronic circuits based on metal nanoparticles. Nat Nanotechnol 2016;11:603–8.

[11] Choi DS, Robertson AW, Warner JH, et al. Low-temperature chemical vapor deposition synthesis of Pt-Co alloyed nanoparticles with enhanced oxygen reduction reaction catalysis. Adv Mater 2016;28:7115–22.

[12] Miura H, Tanaka Y, Nakahara K, et al. Concerted catalysis by adjacent palladium and gold in alloy nanoparticles for the versatile and practical [2+2 +2] cycloaddition of alkynes. Angew Chem Int Ed 2018;57:6136–40.

[13] Wang J, Chang X, Chen S, et al. On the role of sn segregation of Pt-Sn catalysts for propane dehydrogenation. ACS Catal 2021;11:4401–10.

[14] Kim K, Min K, Go Y, et al. FeCo alloy nanoparticles embedded in N-doped carbon supported on highly defective ketjenblack as effective bifunctional electrocatalysts for rechargeable Zn-air batteries. Appl Catal B-Environ 2022;315:121501.

[15] Lee J, Yeon C, Oh J, et al. Highly active and stable catalyst with exsolved PtRu alloy nanoparticles for hydrogen production via commercial diesel reforming. Appl Catal B-Environ 2022;316:121645.

[16] Ye K, Cao A, Shao J, et al. Synergy effects on Sn-Cu alloy catalyst for efficient CO_2 electroreduction to formate with high mass activity. Sci Bull 2020;65:711–9.

[17] Goudeli E, Pratsinis SE. Surface composition and crystallinity of coalescing silver-gold nanoparticles. ACS Nano 2017;11:11653–60.

[18] Zaleska-Medynska A, Marchelek M, Diak M, et al. Noble metal-based bimetallic nanoparticles: the effect of the structure on the optical, catalytic and photocatalytic properties. Adv Colloid Interface Sci 2016;229:80–107.

[19] Zhan W, Wang J, Wang H, et al. Crystal structural effect of AuCu alloy nanoparticles on catalytic CO oxidation. J Am Chem Soc 2017;139:8846–54.

[20] Park J, Kim D, Byun SW, et al. Impact of Pd:Pt ratio of Pd/Pt bimetallic catalyst on CH_4 oxidation. Appl Catal B-Environ 2022;316:121623.

[21] Qiu T, Cheng J, Liang Z, et al. Unveiling the nanoalloying modulation on hydrogen evolution activity of ruthenium-based electrocatalysts encapsulated by B/N co-doped graphitic nanotubes. Appl Catal B-Environ 2022;316:121626.

[22] El Sawy EN, Handal HT, Thangadurai V, et al. Pt_xIr_y alloy nanoparticles with fully tunable bulk and surface compositions. J Mater Chem A 2016;4:15400–10.

[23] van Etten MPC, Zijlstra B, Hensen EJM, et al. Enumerating active sites on metal nanoparticles: understanding the size dependence of cobalt particles for CO dissociation. ACS Catal 2021;11:8484–92.

[24] Zhao M, Chen Z, Shi Y, et al. Kinetically controlled synthesis of rhodium nanocrystals with different shapes and a comparison study of their thermal and catalytic properties. J Am Chem Soc 2021;143:6293–302.

[25] Yang M, Jiao L, Dong H, et al. Conversion of bimetallic mof to Ru-doped Cu electrocatalysts for efficient hydrogen evolution in alkaline media. Sci Bull 2021;66:257–64.

[26] Madkour M, Bumajdad A, Al-Sagheer F. To what extent do polymeric stabilizers affect nanoparticles characteristics? Adv Colloid Interface Sci 2019;270:38–53.

[27] Zhong R-Y, Sun K-Q, Hong Y-C, et al. Impacts of organic stabilizers on catalysis of Au nanoparticles from colloidal preparation. ACS Catal 2014;4:3982–93.

[28] Lei H, Wang Z, Yang F, et al. NiFe nanoparticles embedded N-doped carbon nanotubes as high-efficient electrocatalysts for wearable solid-state Zn-air batteries. Nano Energy 2020;68:104293.

[29] Li T, Dong Q, Huang Z, et al. Interface engineering between multi-elemental alloy nanoparticles and a carbon support toward stable catalysts. Adv Mater 2022;34:e2106436.

[30] Huang H, Yan M, Yang C, et al. Graphene nanoarchitectonics: recent advances in graphene-based electrocatalysts for hydrogen evolution reaction. Adv Mater 2019;31:e1903415.

[31] Liu M, Zhang L, Little MA, et al. Barely porous organic cages for hydrogen isotope separation. Science 2019;366:613–20.

[32] Tozawa T, Jones JT, Swamy SI, et al. Porous organic cages. Nat Mater 2009;8:973–8.

[33] Wang H, Jin Y, Sun N, et al. Post-synthetic modification of porous organic cages. Chem Soc Rev 2021;50:8874–86.

[34] Yang X, Sun J-K, Kitta M, et al. Encapsulating highly catalytically active metal nanoclusters inside porous organic cages. Nat Catal 2018;1:214–20.

[35] Zhang G, Mastalerz M. Organic cage compounds–from shape-persistency to function. Chem Soc Rev 2014;43:1934–47.

[36] Hasell T, Cooper AI. Porous organic cages: soluble, modular and molecular pores. Nat Rev Mater 2016;1:16053.

[37] Mastalerz M. Porous shape-persistent organic cage compounds of different size, geometry, and function. Acc Chem Res 2018;51:2411–22.

[38] Gao S, Liu Y, Wang L, et al. Incorporation of metals and enzymes with porous imine molecule cages for highly efficient semiheterogeneous chemoenzymatic catalysis. ACS Catal 2021;11:5544–53.

[39] Singh A, Verma P, Samanta D, et al. Stabilization of ultra-small gold nanoparticles in a photochromic organic cage: modulating photocatalytic CO_2 reduction by tuning light irradiation. J Mater Chem A 2021;9:5780–6.

[40] Hasell T, Zhang H, Cooper AI. Solution-processable molecular cage micropores for hierarchically porous materials. Adv Mater 2012;24:5732–7.

[41] Liu M, Little MA, Jelfs KE, et al. Acid- and base-stable porous organic cages: shape persistence and ph stability via post-synthetic "tying" of a flexible amine cage. J Am Chem Soc 2014;136:7583–6.

[42] Song LN, Zou LC, Wang XX, et al. Realizing formation and decomposition of Li_2O_2 on its own surface with a highly dispersed catalyst for high round-trip efficiency $Li-O_2$ batteries. iScience 2019;14:36–46.

[43] Zhang Y, Liu X, Li P, et al. Dopamine-crosslinked TiO_2/perovskite layer for efficient and photostable perovskite solar cells under full spectral continuous illumination. Nano Energy 2019;56:733–40.

[44] Zhu Y, Bu L, Shao Q, et al. Subnanometer PtRh nanowire with alleviated poisoning effect and enhanced C–C bond cleavage for ethanol oxidation electrocatalysis. ACS Catal 2019;9:6607–12.

[45] Peng W, Jin J, Yang S, et al. Hollow Co_9S_8 spheres-derived polyhedrons uniformly anchored on N, S-doped graphene for efficient oxygen electrocatalysts. Compos Commun 2021;23:100587.

[46] Tang X, Wu Y, Zhai W, et al. Iron-based nanocomposites implanting in N, P co-doped carbon nanosheets as efficient oxygen reduction electrocatalysts for Zn-air batteries. Compos Commun 2022;29:100994.

[47] Zheng Y, Ni X, Li K, et al. Multi-heteroatom-doped hollow carbon nanocages from ZIF-8@CTP nanocomposites as high-performance anodes for sodium-ion batteries. Compos Commun 2022;32:101116.

[48] Yan Q, Wang XY, Feng JJ, et al. Simple fabrication of bimetallic platinum-rhodium alloyed nano-multipods: A highly effective and recyclable catalyst for reduction of 4-nitrophenol and rhodamine b. J Colloid Interface Sci 2021;582:701–10.

[49] Vellaichamy B, Periakaruppan P. Silver nanoparticle-embedded rgo-nanosponge for superior catalytic activity towards 4-nitrophenol reduction. RSC Adv 2016;6:88837–45.

[50] Liu Y, Dong H, Huang H, et al. Electron-deficient Au nanoparticles confined in organic molecular cages for catalytic reduction of 4-nitrophenol. ACS Appl Nano Mater 2022;5:1276–83.

[51] Sun JK, Zhan WW, Akita T, et al. Toward homogenization of heterogeneous metal nanoparticle catalysts with enhanced catalytic performance: soluble porous organic cage as a stabilizer and homogenizer. J Am Chem Soc 2015;137:7063–6.

[52] Cheng N, Norouzi Banis M, Liu J, et al. Atomic scale enhancement of metal–support interactions between Pt and ZrC for highly stable electrocatalysts. Energy Environ Sci 2015;8:1450–5.

[53] Gao W, Zhang Z, Dou M, et al. Highly dispersed and crystalline Ta_2O_5 anchored Pt electrocatalyst with improved activity and durability toward oxygen reduction: promotion by atomic-scale $Pt-Ta_2O_5$ interactions. ACS Catal 2019;9:3278–88.

[54] Cong C, Nakayama S, Maenosono S, et al. Microwave-assisted polyol synthesis of Pt/Pd and Pt/Rh bimetallic nanoparticles in polymer solutions prepared by batch and continuous-flow processing. Ind Eng Chem Res 2017;57:179–90.

Hele Guo received his B.S. and Master's degrees from Donghua University in 2017 and 2020, respectively. He is now a Ph.D. candidate at the Department of Chemistry, KU Leuven. His main research interest focuses on the field of controllable preparation of carbon hybrid materials or high-entropy materials for advanced energy conversion and storage.

Yali Liu received her Master's degree from Donghua University in 2022. Her main research interest mainly focuses on the preparation of molecular cage-confined metal nanoparticles and their applications in catalysis.

Hongliang Dong received his B.S. degree from Dalian Jiaotong University (2006), Master's degree from Dalian Jiaotong University (2009), and Ph.D. degree from Shanghai Institute of Ceramics, Chinese Academy of Sciences (2013). He is now a specialist associate staff scientist at Center for High Pressure Science and Technology Advanced Research (HPSTAR). His main research interest includes high pressure science and technology, advanced energy conversion materials and devices, nano films and membranes, high entropy materials and synchrotron radiation.

Tianxi Liu obtained his B.S. degree from Henan University (1992) and Ph.D. degree from Changchun Institute of Applied Chemistry, Chinese Academy of Sciences (1998). He is currently a full professor at Jiangnan University. His main research interest includes polymer nanocomposites, organic/inorganic hybrid materials, nanofibers and their composites, advanced energy materials and energy conversion and storage.

Feili Lai received his B.S. degree from Donghua University (2014), Master's degree from Fudan University (2017), and Ph.D. degree from Max Planck Institute of Colloids and Interfaces/Universität Potsdam (2019). He is now a research fellow at the Department of Chemistry, KU Leuven. His current interest includes the 4D soft robotics, the design and synthesis of low-dimensional solids for energy storage and conversion applications.